Supracrystalline Colloidal Eggs: Epitaxial Growth and Freestanding Three-Dimensional Supracrystals in Nanoscaled Colloidosomes

Zhijie Yang,[†] Thomas Altantzis,[‡] Daniele Zanaga,[‡] Sara Bals,[‡] Gustaaf Van Tendeloo,[‡] and Marie-Paule Pileni*,[§]

[†]Université Paris Diderot, Sorbonne Paris Cité, ITODYS, UMR 7086 CNRS, 15 Rue J-A de Baïf, 75205, Cedex 13 Paris, France
[‡]Electron Microscopy for Materials Research (EMAT), University of Antwerp, Groenenborgerlaan 171, 2020 Antwerp, Belgium
[§]CEA/IRAMIS, CEA Saclay F-91191 Gif-sur-Yvette, France

S *Supporting Information*

ABSTRACT: The concept of template-confined chemical reactions allows the synthesis of complex molecules that would hardly be producible through conventional method. This idea was developed to produce high quality nanocrystals more than 20 years ago. However, template-mediated assembly of colloidal nanocrystals is still at an elementary level, not only because of the limited templates suitable for colloidal assemblies, but also because of the poor control over the assembly of nanocrystals within a confined space. Here, we report the design of a new system called "supracrystalline colloidal eggs" formed by controlled assembly of nanocrystals into complex colloidal supracrystals through superlattice-matched epitaxial overgrowth along the existing colloidosomes. Then, with this concept, we extend the supracrystalline growth to lattice-mismatched binary nanocrystal superlattices, in order to reach anisotropic superlattice growths, yielding freestanding binary nanocrystal supracrystals that could not be produced previously.
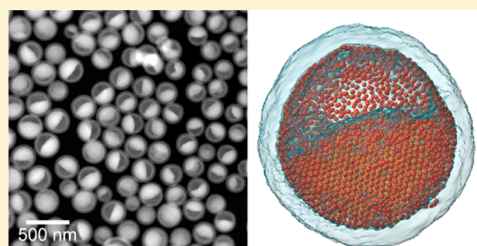
INTRODUCTION

More than a century has passed since Pickering and Ramsden investigated paraffin–water emulsions with microsized particles and discovered that these solid particles could stand at the interface between two immiscible fluids.[1] Later on, this conceptual idea was applied to produce colloidosomes with their shell consisting of densely packed particles.[2,3] In principle, colloidosomes are made at a liquid–liquid interface, a region where the particles are highly mobile and can rapidly reach equilibrium through assemblies that minimize the *Helmholtz* free energy.[3] The force is considerable driving the micrometer-sized particles to adsorb at the interfaces between immiscible liquids, whereas it decreases markedly for small sized nanocrystals with energy of thermal fluctuations comparable to the liquid–liquid interfacial energy.[4,5] Hence, the design of nanoscaled colloidosomes with a nanocrystal shell, although challenging, may be critical in generating new properties.

Colloidal crystallization of nanocrystals leading to a three-dimensional nanocrystal ordering (supracrystals) is of particular importance toward the fabrication of new devices, and it is conventionally divided into two categories: evaporation driven sedimentation on a substrate and destabilization driven precipitation in solution.[6,7] However, during spontaneous colloidal assembly, it is often difficult to precisely achieve desired crystal domains and crystal shapes. Recently, colloidal icosahedral supraparticles made from hydrophobic nanocrystals have been successfully produced by spherical confinement,[8,9] but an important limitation remains since emulsion droplets

used for the directed assembly of nanocrystals shrink during the removal of the solvent, which limits the growth of highly complex colloidal superstructures other than the spherical assemblies. Moreover, in comparison to single component colloidal supracrystals, the assembly of free-standing binary nanocrystal supracrystals made of two distinct types of nanocrystals is increasingly more complicated due to several competing forces within the system such as dipolar, Coulombic, or van der Waals forces.[10−15] It was demonstrated that it is impossible to produce binary nanocrystal supracrystals through destabilization method in colloidal solutions. Size-segregation of single-component supracrystals occurs, depending on their *Hamaker* constant, which is correlated to *van der Waals* interactions. Hence, the production of colloidal binary nanocrystal supracrystals in liquid phase free of any substrate remains challenging, despite recent advances in the growth of binary nanocrystal superlattices films on a flexible liquid substrate.[16] Thus, the design of a rigid and robust template may provide valuable insights for the construction of highly complex colloidal suprastructures. Here, inspired by the concept of "microreactor", we propose a strategy for the design of nanoscaled colloidosome that can be considered as a reservoir for supracrystals growth in rigid confined geometries. After the supracrystal growth process, a new yolk/shell suprastructure, called supracrystalline colloidal eggs, was
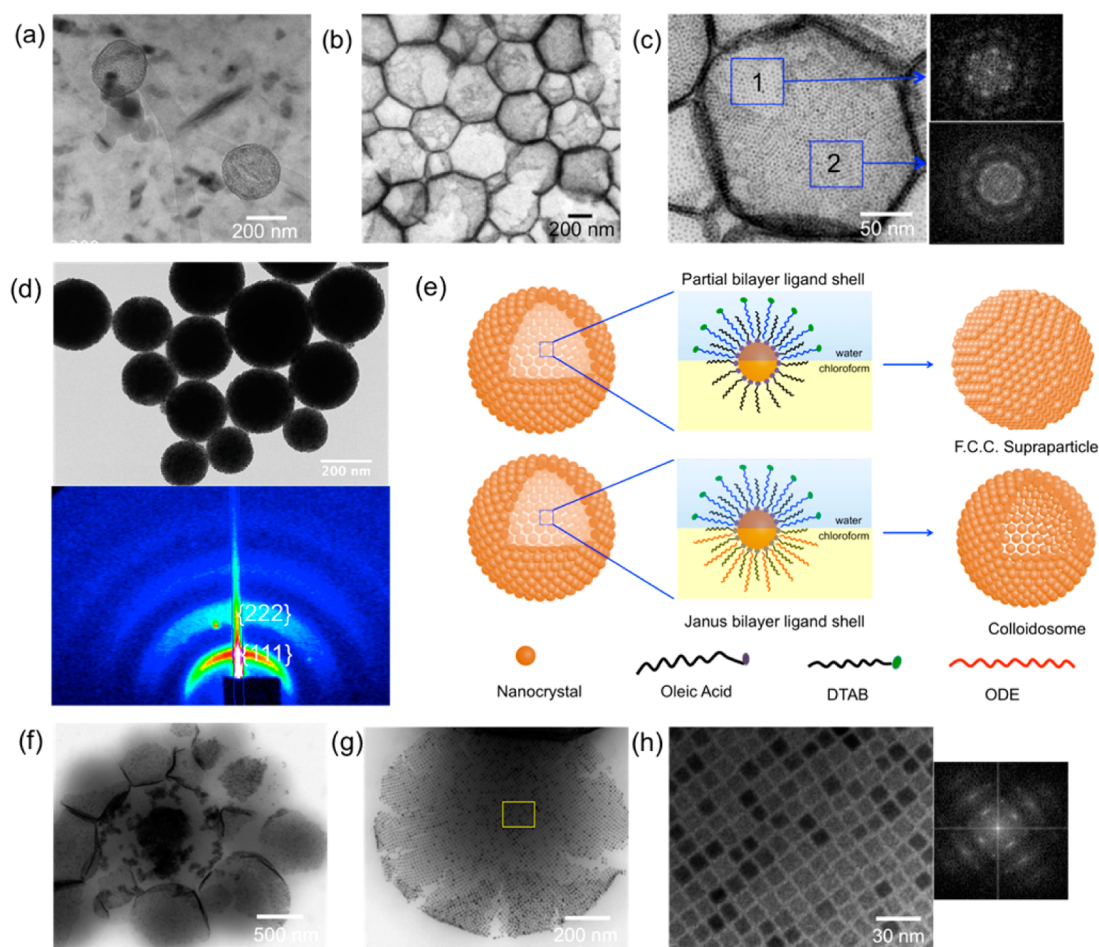
Figure 1. (a) Cryo-TEM image of colloidosome. (b) Low magnification TEM image of the colloidosomes after drying process on copper grids coated with carbon film. (c) High-magnification TEM image of one colloidosome; insets are the corresponding Fast Fourier Transform (FFT) patterns from the selected monolayer and bilayer regions indicated by the black squares. (d) TEM image of the assemblies in the absence of ODE molecules, keeping the other conditions constant; inset is the corresponding SAXS pattern. (e) Schematic illustration of the formation mechanism of nanoscaled colloidosomes: a key step is to form the Janus bilayer on the nanocrystal surfaces. (f−h) TEM images of nanoscaled colloidosomes assembled from Fe_3O_4 nanocubes.

formed. This general synthetic approach enables us to avoid complicated procedures, such as those found in nanocrystal polymersomes.[17,18]

RESULTS AND DISCUSSION

We utilize oil-in-water (O/W) emulsion technique for the fabrication of colloidosomes (Scheme S1, Supporting Information). A key feature of our concept is to transfer the hydrophobic nanocrystals coated with aliphatic chain from inner oil phase to the oil/water interface, and to lock the nanocrystals at the liquid−liquid interface. Instead of using cross-linking agent to achieve additional surface functionalization, we create a "Janus bilayer" shell for the nanocrystals adsorbed at the liquid−liquid interface. For this purpose, Fe_3O_4 spherical nanocrystals coated with aliphatic ligand (oleic acid) were produced from thermal decomposition of iron oleate (Figure S1, Supporting Information) and characterized by 6.5 nm and 6% average diameter and size polydispersity, respectively.[19] With the emulsification of 1 mL of 18 mg/mL aqueous surfactant (i.e., dodecyltrimethylammonium bromide, DTAB) solution and the oil phase containing 300 μL of chloroform of 15 mg/mL Fe_3O_4 nanocrystals and 8 μL of octadecene (ODE), these hydrophobic nanocrystals tend to

adsorb on the droplet interface. This process is spontaneous and is driven by the sum of interfacial energy and the *van der Waals* interactions between the hydrophobic chains of the surfactant and the hydrophobic chain of the surface ligands anchored to the nanocrystals. To stabilize the emulsion, 5 mL of ethylene glycol solution containing 0.4 g of polyvinylpyrrolidone (PVP, $M_w = 40\ 000$) was added swiftly and stirred with a vortex for 30 s. The emulsion was then heated to 70 °C under nitrogen atmosphere and kept at this temperature for 15 min to evaporate the inner chloroform phase (Scheme S1, Supporting Information). The resulting nanocrystal assemblies were washed twice with ethanol and dispersed in deionized water to form stable colloids. To illustrate these nanocrystal assemblies in their native environment, in Figure 1a we show cryo-transmission electron microscopy (cryo-TEM) image of typical spherical colloidosomes dispersed in water without any coalescence. In fact, these colloidosomes are highly stable and do not show any collapse when suspended in water for over six months. After evaporation of the water solvent, two-dimensional (2D) TEM images were recorded on TEM grid; interconnected colloidosomes could be observed forming a Voronoi pattern (Figure 1b). This refers to, during the solvent evaporation process, the viscoelastic characteristics of the
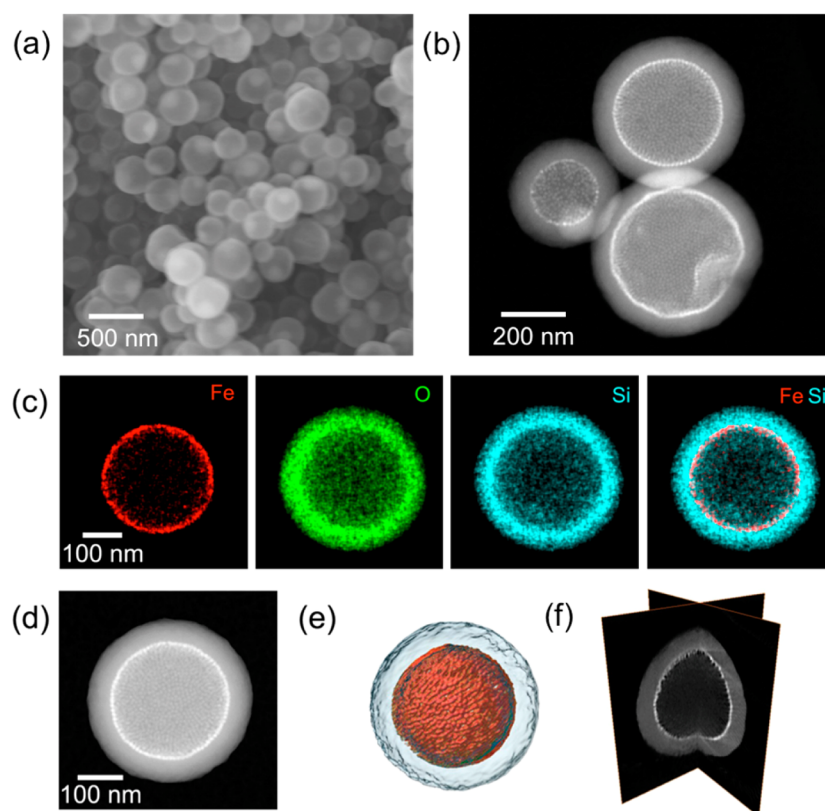
Figure 2. (a) SEM image of colloidosomes; (b) HAADF-STEM overview of the colloidosomes; (c) the STEM-EDS maps revealing the distribution of elements; (d) 2D STEM projection from the tomography series; (e) 3D volume rendering of the SIRT tomographic reconstruction; (f) orthogonal slices from panel e.

colloidal assemblies.[20] It is interesting that the coarsening of these Fe_3O_4 colloidosomes resembles the coarsening of soap bubbles. The latter is mainly attributed to the gas diffusion between bubbles submitted to various pressures. From the magnified TEM image of a typical deflated colloidosome (Figure 1c), it can be observed that Fe_3O_4 nanocrystals maintain their integrities and are self-assembled in compact hexagonal networks. Of particular interest is that the colloidosome is composed of a monolayer shell with hexagonally packed Fe_3O_4 nanocrystals, as confirmed in zone 1 of broken spot in Figure 1c and the corresponding Fast Fourier transform (FFT) pattern. In additon, this monolayer shell of the colloidosome is further confirmed by zone 2 with a bilayer structure induced by deflation of the colloidosome (Figure 1c).

In a drying droplet, an inward move of oil/water interface occurs and redistributes the nanocrystals to a densely packed structure without any hollow interior in a drying process as predicted by the Peclect number.[21,22] Hence, the clear emergence of monolayer−nanocrystal−shell colloidosome is interesting. We believe that the presence of small quantity of aliphatic ODE ($C_{18}H_{36}$) molecules is of particular importance in the formation of colloidosomes. In the absence of ODE molecules, while keeping the other conditions unchanged, the colloidosomes do not form. Instead, large spherical dense-packed assemblies of nanocrystals are produced (Figure 1d). These spherical assemblies were characterized by small-angle X-ray scattering (SAXS). Two typical rings indexed as {111} and {222} can be found in the SAXS pattern (inset in Figure 1d, the line profile is given in Figure S2, Supporting Information), indicative of a face-centered cubic (fcc) packing mode. Keeping

the experimental conditions as described above but replacing ODE with a longer chain molecule, i.e., squalane ($C_{30}H_{50}$, Figure S3 and Scheme S2, Supporting Information), colloidosomes can still be produced, whereas in the presence of a molecule with shorter chain such as dodecane ($C_{12}H_{26}$), the formation of cage-like structures are observed, attributed to the partial shrinkage of the nanocrystal membranes (Figure S4, Supporting Information). These data suggest that specific interactions between aliphatic ODE (and/or squalane) and oleic acid, covalently bounded at the nanocrystals surface, take place. This induces the formation of a monolayer−nanocrystal−membrane at the chloroform/water interface, favoring the colloidosome formation. Hence, the ability to control the amphiphilic balance (Janus balance) of nanocrystals at the liquid−liquid interface seems to be a key mechanism that could drive the colloidosome formation.[23−25] We create a "Janus bilayer shell" on the nanocrystals adsorbed at the liquid−liquid interface as shown in Figure 1e. The inner shell of the bilayer is the tail part of oleic acid covalently bonded to Fe_3O_4, whereas the outer shell is composed of DTAB in the water phase and ODE in the chloroform phase. The formation of such "Janus bilayer shell" on the nanocrystals can immobilize the nanocrystals at the water/chloroform interface in a drying droplet, which is probably achieved by decreasing the diffusion rate of the nanocrystals in the liquid. In contrast, the water/chloroform interface moves inward and the interfacial nanocrystals tend to form densely packed fcc assemblies in the absence of Janus bilayer shell. To confirm that the Janus bilayer shell structure on the interfacial nanocrystals is indispensable for the formation of colloidosomes, we used bulky aromatic molecules (i.e., diphenyl ether) instead of the aliphatic molecules. The result

shows that densely packed nanocrystal assemblies are produced (Figure S5, Supporting Information). This can be explained by the intolerable penetration of bulky molecules into the interspace between the neighboring alkyl chains, hampering the formation of Janus bilayer shell.

The creation of Janus bilayer shell on the nanocrystals is not particularly size sensitive. For instance, increasing the Fe_3O_4 nanocrystals size from 6.5 to 10 nm, while keeping the same experimental conditions, led to the formation of similar colloidosomes (Figure S6, Supporting Information). Furthermore, the formation of Janus bilayers is also valid for other nonspherical nanocrystals. For instance, when spherical Fe_3O_4 nanocrystals are replaced by their cubic counterparts,[26] with an average edge length and distribution of 14.4 nm and 8%, stable colloidosomes of cubic nanocrystals (Figure 1f and Figure S7, Supporting Information) are formed. However, drop casting such aqueous solution on a TEM grid shows that the colloidosomes tend to collapse during the drying process (Figure 1f). This can be attributed to a nanocrystal shape effect. A stronger face-to-face interaction between neighboring nanocubes favors the formation of planar organization instead of the spherical one. However, the nanocubes remain highly ordered as shown in Figure 1g,h with specific facet to facet interactions. Similar results are obtained for $CoFe_2O_4$ nanocubes with similar edge length (13.2 ± 1.0 nm, Figure S8, Supporting Information).

To enhance the robustness of the colloidosomes shell, a silica overcoat procedure was used. The latter assures the colloidal stability during the drying process when depositing on a TEM grid.[27] Figure 2a shows typical Scanning Electron Microscopy (SEM) image of spherical silica coated colloidosomes without any collapse. The average diameter, determined by counting more than 200 colloidosomes, is 430 ± 65 nm (Figure S9, Supporting Information). Low magnification 2D High Angle Annular Dark Field Scanning TEM (HAADF-STEM) images suggest that most of the Fe_3O_4 nanocrystals are located at the periphery of the colloidosomes (Figure 2b), corresponding to a hollow interior. X-ray Energy Dispersive Spectroscopy (STEM-EDS) reveals the formation of a double shell with an outer ~40 nm silica layer and an inner ~7 nm Fe_3O_4 nanocrystal monolayer (Figure 2c). To confirm the hollow structure of the colloidosomes and probe the nanocrystal ordering in the shell, HAADF-STEM tomography was applied. A 2D projection image from the tilt series is presented in Figure 2d. A volume rendering of the obtained 3D reconstruction (Figure 2e), as well as slices through the 3D data set (Figure 2f) confirm the hollow structure of the assemblies. A 3D animation of the reconstructed volume is presented in the Supporting Information Movie 1.

Next, we consider the case with excessive free hydrophobic Fe_3O_4 nanocrystals inside the oil droplets by increasing the amount of Fe_3O_4 nanocrystals from ~15 to ~30 mg/mL while keeping similar experimental conditions. The HAADF-STEM image in Figure 3a shows the colloidosomes coated with a silica layer. In this case, the suprastructure is semihollow, with nanocrystals aggregates filling one side of the inner cavity. SAXS pattern (inset in Figure 3a, the line profile is given in Figure S10, Supporting Information) corresponds to fcc packing of the nanocrystals in the ensemble assemblies.[28] HAADF-STEM images (Figure 3b) suggest that the aggregates yield a crystalline structure. Lattice fringes within the inner phase are clearly observed from STEM-HAADF images (Figure 3b). Further investigation by electron tomography (Figure
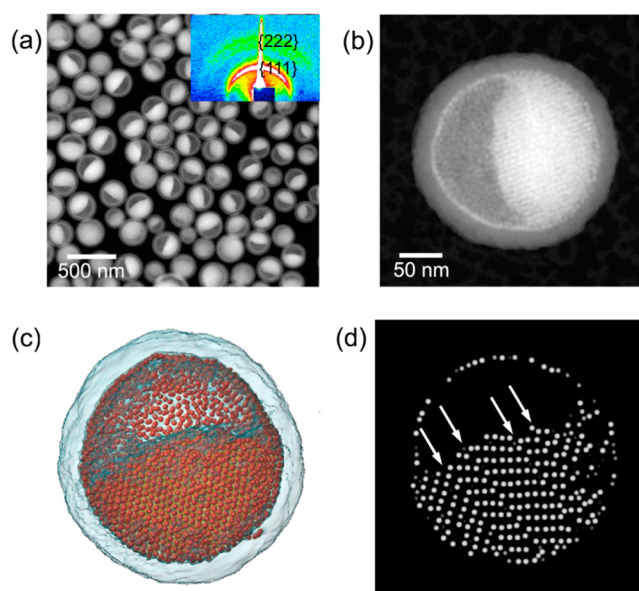

Figure 3. (a) HAADF-STEM overview image of the half-filled colloidosomes, inset in (a) is the corresponding SAXS pattern; (b) 2D HAADF-STEM projection image from the tilt series; (c) 3D representation of the SSR reconstruction; (d) orthoslice from the SSR reconstruction, highlighting different defects in the nanocrystals stacking (white arrows).

3c,d) confirms the presence of ordered stackings of particles inside the assemblies. STEM-EDS reveals that Si is mainly located in the surrounding shell of the spherical colloidosomes (Figure S11, Supporting Information).

A thorough analysis of the 3D structure of the assembly is performed using the so-called "Sparse Sphere Reconstruction" (SSR) algorithm. Through this algorithm, it is possible to extract the coordinates of every single spherical particle in the assembly. In this manner, local bond order parameters were calculated, showing an overall fcc packing mode. However, defects can clearly be observed by inspecting slices through the reconstruction (Figure 3d), resulting in a disordered stacking in certain areas. The movie of such structure can be found in Supporting Information Movie 2. TEM images suggest that the inner 3D superlattices are oriented along the outer monolayer nanocrystal shell, resembling an integrated single domain feature (Figure 4), revealing an epitaxial growth as already observed for heterostructure with matched lattices in atomic solids.[29,30] Therefore, we can conclude that epitaxial overgrowth of 3D supracrystals on colloidosome occurs,[31] giving a conformal semihollow suprastructure. In addition, as observed under heterogeneous growth process, the supracrystals grown by epitaxial growth process is also faceted (Figure 4b,d,f). This suggests that these colloidosome shells are moldable during the epitaxial overgrowth process, originating from its viscoelastic characteristics.

From these observations, it can be concluded that densely packed fcc supracrystals epitaxially grow inside the colloidosomes. It could be assumed that this process is driven by minimization of the free volume entropy. It should be stressed that fully filled supracrystals (solid) cannot be produced in the presence of aliphatic molecules, like ODE and/or squalane. Hence, it seems reasonable to conclude that the formation of Janus bilayer shell on nanocrystals is responsible for the formation of colloidosomes and the subsequent epitaxial growth of the supracrystals on the interfacial nanocrystal
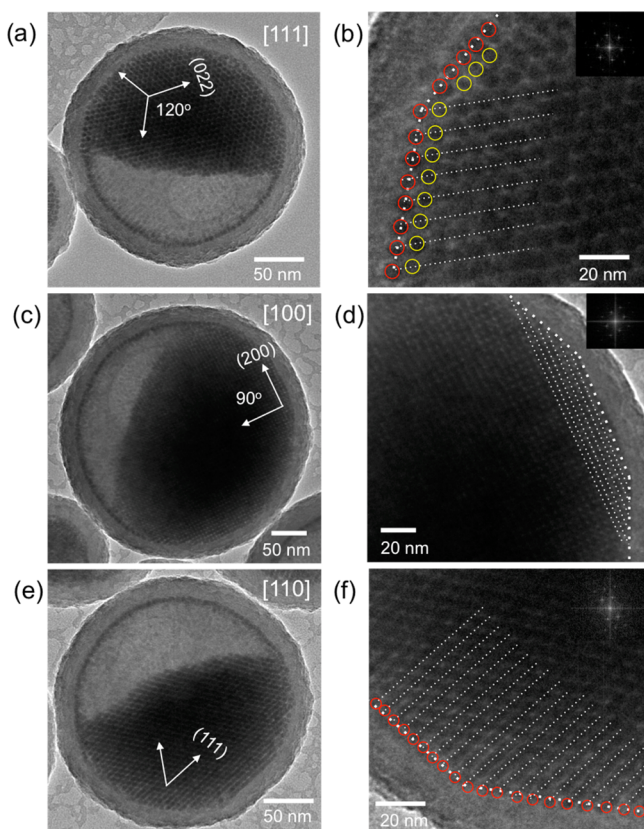
Figure 4. (a) TEM image of a half-full colloidosome viewed along the [111] zone axis and (b) is enlarged area in (a); (c) TEM image of a half-full colloidosome viewed along the [100] zone axis and (d) is enlarged area in (c); (e) TEM image of a half-full colloidosome viewed along the [110] zone axis and (f) is enlarged area in (e). The red cycles in (b) and (f) indicate the outmost arrangement of Fe_3O_4 supracrystals, while the yellow cycles in (b) indicate the second layer of Fe_3O_4 supracrystals. The dashed line in (b), (d), and (f) indicates the conformal structure of such supracrystals.

membrane. The relatively large amount of Fe_3O_4 nanocrystals coated with oleic acid favor the supracrystal growth. This shows that single-component fcc supracrystals are highly attached to the colloidosome surfaces and consequently permit to grow hydrophobic supracrystals in hydrophilic environments.

It is known that mixtures of hydrophobic nanocrystals, having two well-defined sizes, with a low size distribution, self-assemble into binary nanocrystal superlattices.[32,33] The key factor to produce such assemblies is the size ratio γ between large and small particles in the binary mixture. The ratio γ is given by $\gamma = d_{eff(small)}/d_{eff(large)}$, where d_{eff} is the effective diameter, defined as the center-to-center distance between nanocrystals (small or large) self-ordered in a compact hexagonal network. With the use of a hard sphere model based on the ratio γ, the structure of binary systems can be predicted.[34] According to the data presented above, we pose the following question: is it possible to realize the growth of binary supracrystals inside the colloidosomes? For this purpose, we combined 6.5 ± 0.3 nm Fe_3O_4 and 3.5 ± 0.2 nm Au nanocrystals coated with oleic acid and dodecanethiol, respectively, with $\gamma = 0.58$. From the hard sphere model and for this γ value, the expected crystalline structures either correspond to $NaZn_{13}$ or AlB_2-type structures.[34]

To engineer the binary supracrystal growth inside the colloidosomes, we use a similar emulsion-based procedure as

described above: 200 μL of 30 mg/mL Fe_3O_4 nanocrystals and 100 μL of 10 mg/mL Au nanocrystals dispersed in the chloroform and 8 μL of ODE solutions were mixed with 1 mL of 18 mg/mL DTAB aqueous solution. At the end of the procedure, the colloidal suspension remained stable. Figure 5a shows a cryo-TEM image of a colloidosome. Its inset shows that the Fe_3O_4 nanocrystals remain at the colloidosome shell as already observed in the absence of Au nanocrystals and shown on Figure 1a. Furthermore, at the center of the colloidosome, a rectangular shaped structure with brighter contrast is formed, yielding supracrystalline colloidal eggs (yolk/shell structure). After evaporation of the carrier solvent, HAADF-STEM characterization (Figure 5b) confirms the presence of both a shell consisting of nanocrystals and a rectangular assembly inside the colloidosomes. A careful analysis of the inner assembly was carried out by HAADF-STEM imaging along the $\langle 001 \rangle_{SL}$ and $\langle 011 \rangle_{SL}$ zone axes (Figure 5b–d,f). These results indicate a $NaZn_{13}$-type $(Fe_3O_4)Au_{13}$ structure (crystal model in Figure 5h), which has been reported for supported films.[35,36] STEM-EDS elemental mapping was applied, and these results further verify the structure (Figure 5e,g). Due to the inherent cubic lattice of the $NaZn_{13}$ structure, anisotropic supracrystal growth occurs, resulting in an anisotropic cuboid of binary supracrystals. Furthermore, due to the large lattice mismatch between $NaZn_{13}$ type binary nanocrystal supracrystals and hexagonal network of nanocrystal monolayer, conformal epitaxial overgrowth of superlattices along the nanocrystal monolayer is forbidden. Hence, multiple nucleation sites are also observed inside a single colloidosome instead of the single supracrystal observed in the case of conformal epitaxy (Figure S12, Supporting Information). Furthermore, it is also known that the final structure can be controlled by the concentration ratio between small and large nanocrystals.[37,38] For instance, increasing the concentration of Au nanocrystals from 10 to 40 mg/mL resulted in the formation of single-component Au supracrystals inside the Fe_3O_4 colloidosomes.
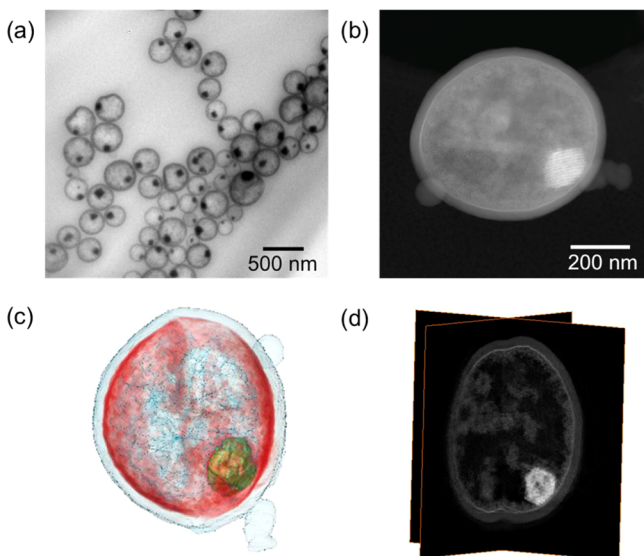
Low-magnification TEM and HAADF-STEM images presented in Figure 6a,b confirm the increased robustness for these colloidosomes after their encapsulation in a silica shell. STEM-EDS elemental mapping (Figure S13, Supporting Information) reveals the presence of Au inside the colloidosomes. Fe is observed in both the periphery as well as inside the assembly, whereas Si is only present in the shell. Electron tomography measurements were used to visualize the yolk/shell heterogeneous structure in 3D (Figure 6c,d). The movie of such structure can be found in Supporting Information. These results confirm the formation of binary supracrystals inside the colloidosomes, which can be attributed to free energy minimization.[39] The size ratio γ provides a good indicator to predict the crystal phases of binary superlattices by evaporation driven sedimentation method. Similarly, an increase of the Fe_3O_4 nanocrystal size to 7.4 nm while maintaining the size of the Au nanocrystals led to the formation of AlB_2-type $(Fe_3O_4)Au_2$ binary nanocrystal supracrystals inside the Fe_3O_4 colloidosomes, as shown by TEM (Figure S14, Supporting Information).

■ CONCLUSIONS

In summary, we have reported a new strategy toward the fabrication of colloidosomes assembled by nanocrystals, with the shape of the nanocrystals not being limited to spheres. Furthermore, we have demonstrated that these colloidosomes can be used as microreactors for the supracrystal growth: from
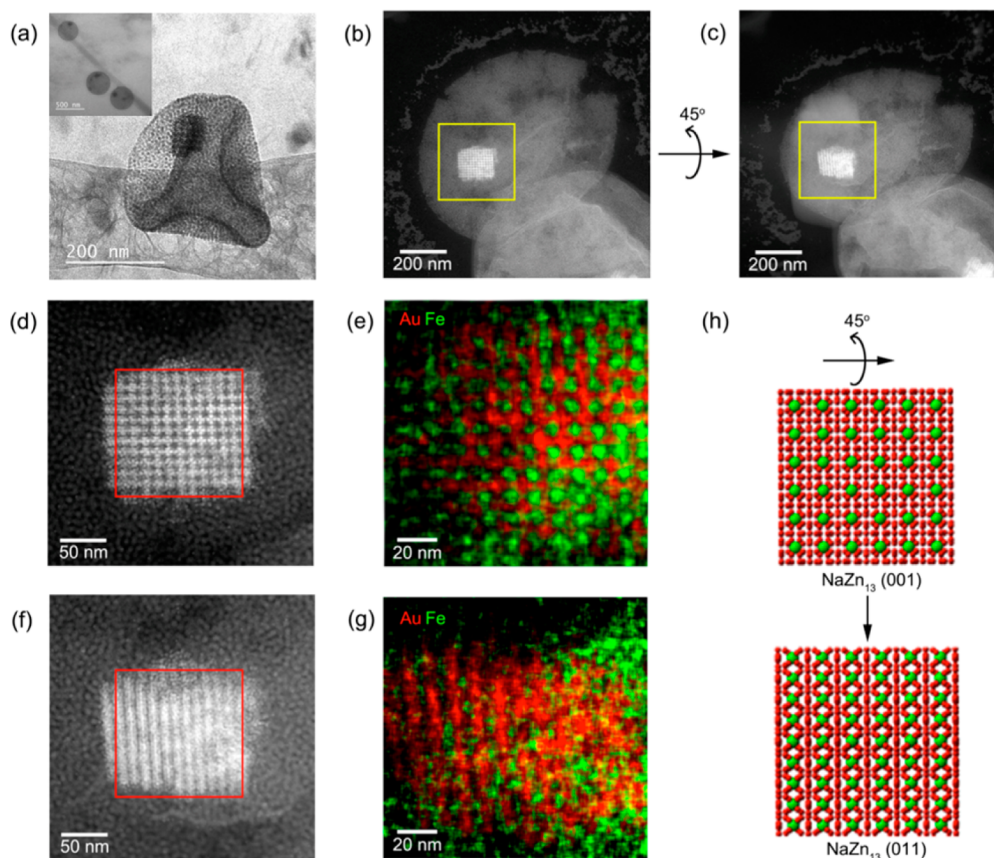
Figure 5. (a) Cryo-TEM image of one single colloidosome assembled from the Fe_3O_4/Au binary mixture. (b and c) HAADF-STEM images of one single colloidosome, showing the cracked structure after the drying process, tilted 45° with respect to each other. (d and f) Enlarged images of the regions indicated by the yellow squares in (b) and (c), respectively. (e and g) STEM-EDS maps from the regions indicated by the red squares in (d) and (f), respectively. (h) Model of the $NaZn_{13}$ structure: a 45° rotation along the *x* axis leads to a transition from a ⟨001⟩ to a ⟨011⟩ zone axis.

Figure 6. (a) Low-magnification TEM image of the colloidosomes with binary supracrystals; (b) low-magnification HAADF-STEM image of yolk/shell colloidosomes coated by a silica layer; (c) 3D volume rendering of the SIRT reconstruction of a single colloidosome; (d) orthogonal slices through it.

the superlattice-match conformal epitaxial overgrowth to the superlattice-mismatch growth of binary supracrystals, yielding complex assemblies like colloidal eggs. Our findings provide

insights into the new applications of colloidosomes and into the design of nanocrystal-based dispersible multifunctional materials for biomedicine.

■ EXPERIMENTAL SECTION

Chemicals. All chemicals were used as received without any further purification: iron(III) chloride hexahydrate (Sigma-Aldrich, 97%), oleic acid (Sigma-Aldrich, >90%), chloroform (Sigma-Aldrich, ≥99.5%), isopropyl alcohol (Aldrich, ≥99.7%), hexane (Sigma-Aldrich, 95%), toluene (Sigma-Aldrich, 99.8%), tetraethyl orthosilicate (TEOS, Aldrich, 99.999%), ammonia solution (VWR, 27–30%), anhydrous ethanol (VWR, 99%), ethylene glycol (Sigma-Aldrich, 99.8%), dodecanethiol (Aldrich, ≥98%), 1-octadecene (Aldrich, 90%), dioctyl ether (Aldrich, 99%), dodecyltrimethylammonium bromide (TCI, >98%), squalane (Aldrich, 99%), dodecane (Sigma-Aldrich, ≥99%), chlorotriphenylphosphine Au(I) (Strem, 99.9%), borane *tert*-butylamine complex (Aldrich, 97%), sodium oleate (TCI, >97%), and polyvinylpyrrolidone (PVP40, Sigma-Aldrich).

Apparatus. Conventional transmission electron microscopy (TEM) was performed using a JEOL 1011 microscope at 100 kV. High-resolution transmission electron microscopy was performed using a JEOL 2010 microscope at 200 kV. High-resolution scanning electron microscopy (HRSEM) images were obtained with Hitachi Su-70 instrument.

Cryo-TEM imaging was performed using a JEOL 2010 transmission electron microscope operating at 200 kV. Liquid samples (8 μL) were dropped on a lacey carbon film covered copper grid. The thin film specimens were instantly shock frozen by rapid immersion into liquid ethane and cooled to approximately 90 K by liquid nitrogen in a temperature-controlled freezing unit. After ethane was removed, the

frozen samples were inserted into a cryo transfer holder. The imaging studies were carried out at temperatures around 90 K.

2D and 3D HAADF-STEM measurements were performed using an aberration-corrected cubed FEI-Titan 60-300 electron microscope operated at 200 kV. For the acquisition of the tomography series, a Fischione model 2020 singe tilt holder was used and all series were acquired using a tilt range from −74° to +74° and an increment of 2°. The acquisition was performed in HAADF-STEM mode in order to avoid unwanted diffraction contrast.

The alignment of the series was performed using cross-correlation routines[40] implemented in Matlab, and the reconstruction was performed using the Simultaneous Iterative Reconstruction Technique (SIRT)[41] from the ASTRA toolbox,[42,43] and the SSR technique, also implemented in Matlab as described by Zanaga et al.[44]

2D EDS measurements were performed using an aberration-corrected cubed FEI-Titan 60-300 electron microscope operated at 200 kV equipped with a ChemiSTEM system.[45]

Small-angle X-ray Scattering (SAXS) measurements are performed with a homemade system with a rotating copper anode generator operated with a small-size focus (0.1 Å to ~0.1 mm^2 in cross section) at 40 kV and 20 mA, and the reading of the exposed imaging plate is performed by a scanner (STORM 820 Molecular Dynamics).

Synthesis of Iron Oxide Nanocrystals. Monodisperse iron oxide nanocrystals are synthesized by modifying the method reported by Hyeon et al.[19] First, iron oleate precursors are prepared as follows: 10.8 g of iron(III) chloride, 36.5 g of sodium oleate, 40 mL of DI water, 40 mL of ethanol, and 80 mL of hexane are mixed into a 500 mL three-neck flask. The mixture is refluxed at 60 °C for 4 h. The dark red-black colored iron oleate precursors are dissolved in 100 mL of hexane. The hexane solution is further washed 3 times by warm DI water (~50 °C) and separated in a separatory funnel. The viscous product is obtained by evaporating the hexane in a rotary evaporator. A stock precursor solution with a concentration of 0.5 mol/kg is prepared by adding 1.5 g of octadecene to each gram of iron oleate.

In a typical synthesis of 6.5 nm Fe$_3$O$_4$ nanocrystals, 4.8 g of precursor solution is mixed with 0.76 g of oleic acid and with 6.0 g of octylether. The mixture is heated to 110 °C and maintained at this temperature for 60 min under N$_2$ protection. Then, the solution is heated to the boiling point of the solution (~295 °C) and is kept at this temperature for 30 min followed by removal of the heater. The colloidal solution is washed 5 times using isopropyl alcohol/hexane (1:1 v/v) by sedimenting and redispersing using centrifugation (5000 rpm for 10 min). Finally, the Fe$_3$O$_4$ nanocrystals are weighted and redispersed in chloroform with desired nanocrystal concentration.

For the synthesis of 14 nm edge length Fe$_3$O$_4$ nanocubes, 4.8 g of precursor solution is mixed with 0.38 g of oleic acid and 0.76 g of sodium oleate in a mixed solvent of 6.0 g of octadecene and 1.0 g of octylether. The mixture is heated to 110 °C and maintained at this temperature for 60 min under N$_2$ protection. Then, the solution is heated to the boiling point of the solution (~305 °C) and is kept at this temperature for 30 min followed by removal of the heater. The colloidal solution is washed 5 times using isopropyl alcohol/hexane (1:1 v/v) by sedimenting and redispersing using centrifugation (5000 rpm for 10 min). Finally, the Fe$_3$O$_4$ nanocrystals are weighted and redispersed in chloroform with desired nanocrystal concentration.

Synthesis of 3.5 nm Au Nanocrystals. Au nanocrystals with 3.5 nm in diameter are synthesized by revisiting the Stucky method. Typically, two solutions are used. One consists of 0.20 mmol of chlorotriphenylphosphine Au(I) dissolved in 25 mL of toluene to which 500 μL of dodecanethiol (DDT) is added, whereas the other one contains 5 mmol of tert-butylamine borane dissolved in 2 mL of toluene. The two solutions are placed in a silicone oil bath at 100 °C and are stirred for 10 min. Subsequently, tert-butylamine borane solution is injected into the solution with gold salt swiftly. The colorless and clear mixture turns to brown and reaches a dark purple-red solution in 1 min, and this solution is kept at 100 °C for another 4 min followed by the removal of the oil bath. The Au nanocrystals are precipitated from the colloidal solution by adding 10 mL of methanol. The supernatant is removed. The black precipitate is dried in a nitrogen flow in order to eliminate the remaining solvent. The Au

nanocrystals are weighted and redispersed in chloroform with desired nanocrystal concentration.

Synthesis of Fe$_3$O$_4$ Colloidosomes. For a typical self-assembly experiment, 3 mg of iron oxide nanoparticles was dispersed in mixed solvent with 200 μL of chloroform and 8 μL of octadecene, and the mixture was added to an aqueous solution containing 18 mg of DTAB. The resulting emulsion was severely agitated by a vortex for 30 s. Subsequently, 5 mL of ethylene glycol solution containing 0.4 g of PVP ($M_w = 40\,000$) was added swiftly into the emulsion and subjected to agitation with a vortex for another 30 s. The emulsion was then heated to 70 °C under N$_2$ protection and kept at this temperature for 15 min to evaporate the inner chloroform phase. The suspension was then allowed to cool to room temperature. The resulting nanoparticle assemblies were washed twice with ethanol and redispersed in DI water.

Synthesis of Fe$_3$O$_4$ Semihollow Suprastructures. For a typical self-assembly experiment, 6 mg of iron oxide nanoparticles was dispersed in mixed solvent with 200 μL of chloroform and 8 μL of octadecene, and the mixture was added to an aqueous solution containing 18 mg of DTAB. The resulting emulsion was severely agitated by a vortex for 30 s. Subsequently, 5 mL of ethylene glycol solution containing 0.4 g of PVP ($M_w = 40\,000$) was added swiftly into the emulsion and subjected to agitation with a vortex for another 30 s. The emulsion was then heated to 70 °C under N$_2$ protection and kept at this temperature for 15 min to evaporate the inner chloroform phase. The suspension was then allowed to cool to room temperature. The resulting nanoparticle assemblies were washed twice with ethanol and redispersed in DI water.

Synthesis of Au/Fe$_3$O$_4$ NaZn$_{13}$ Type Binary Superlattices in Colloidosomes. For a typical self-assembly experiment, 6 mg of 6.5 nm iron oxide nanopcrystals and 1 mg of Au nanocrystals were dispersed in a mixed solvent with 300 μL of chloroform and 8 μL of octadecene, and the mixture was added to an aqueous solution containing 18 mg of DTAB. The resulting emulsion was severely agitated by a vortex for 30 s. Subsequently, 5 mL of ethylene glycol solution containing 0.4 g of PVP ($M_w = 40\,000$) was added swiftly into the emulsion and subjected to agitation with a vortex for another 30 s. The emulsion was then heated to 70 °C under N$_2$ protection and kept at this temperature for 15 min to evaporate the inner chloroform phase. The suspension was then allowed to cool to room temperature. The resulting nanoparticle assemblies were washed twice with ethanol and redispersed in DI water.

For the assembly of AlB$_2$ type binary nanocrystal superlattices, larger sized 7.5 nm Fe$_3$O$_4$ were used. Typically, 6 mg of 7.5 nm Fe$_3$O$_4$ nanocrystals and 1 mg of 3.5 nm were used and subjected to a similar assembly procedure as above.

Silica Coating on the Colloidosomes. For a typical synthesis, ~2 mg of colloidosomes was dissolved in 10 mL of ethanol. Subsequently, 2 mL of DI water and 0.7 mL of ammonia solution were added in the alcoholic colloidosome solution with magnetic stirring (500 rpm). Then, 20 μL of TEOS diluted in 1 mL of ethanol was injected dropwise into the above solution. The final solution was kept stirring for 30 min at room temperature (~298 K). The silica-coated product was isolated by centrifugation (10\,000 rpm for 10 min), washed twice with DI water, and dispersed in 1 mL of ethanol.

■ ASSOCIATED CONTENT

⑤ Supporting Information

The Supporting Information is available free of charge on the ACS Publications website at DOI: 10.1021/jacs.5b13235.

Additional experimental data: Schemes S1 and S2, and Figures S1−14 (PDF)

Movie 1 (MPG)

Movie 2 (MPG)

Movie 3 (MPG)

■ AUTHOR INFORMATION

Corresponding Author
*E-mail: mppileni@orange.fr

Notes
The authors declare no competing financial interest.

■ REFERENCES

(1) Pickering, S. U. *J. Chem. Soc., Trans.* **1907**, *91*, 2001−2021.
(2) Dinsmore, A. D.; Hsu, M. F.; Nikolaides, M. G.; Marquez, M.; Bausch, A. R.; Weitz, D. A. *Science* **2002**, *298*, 1006−1009.
(3) Velev, O. D.; Furusawa, K.; Nagayama, K. *Langmuir* **1996**, *12*, 2374−2384.
(4) Lin, Y.; Skaff, H.; Emrick, T.; Dinsmore, A. D.; Russell, T. P. *Science* **2003**, *299*, 226−229.
(5) Duan, H.; Wang, D.; Sobal, N. S.; Giersig, M.; Kurth, D. G.; Möhwald, H. *Nano Lett.* **2005**, *5*, 949−952.
(6) Bodnarchuk, M. I.; Li, L.; Fok, A.; Nachtergaele, S.; Ismagilov, R. F.; Talapin, D. V. *J. Am. Chem. Soc.* **2011**, *133*, 8956−8960.
(7) Talapin, D. V.; Shevchenko, E. V.; Kornowski, A.; Gaponik, N.; Haase, M.; Rogach, A. L.; Weller, H. *Adv. Mater.* **2001**, *13*, 1868−1871.
(8) de Nijs, B.; Dussi, S.; Smallenburg, F.; Meeldijk, J. D.; Groenendijk, D. J.; Filion, L.; Imhof, A.; van Blaaderen, A.; Dijkstra, M. *Nat. Mater.* **2015**, *14*, 56−60.
(9) Bai, F.; Wang, D.; Huo, Z.; Chen, W.; Liu, L.; Liang, X.; Chen, C.; Wang, X.; Peng, Q.; Li, Y. *Angew. Chem., Int. Ed.* **2007**, *46*, 6650−6653.
(10) Hynninen, A. P.; Christova, C. G.; van Roij, R.; van Blaaderen, A.; Dijkstra, M. *Phys. Rev. Lett.* **2006**, *96*, 138308.
(11) Shevchenko, E. V.; Talapin, D. V.; Kotov, N. A.; O'Brien, S.; Murray, C. B. *Nature* **2006**, *439*, 55−59.
(12) Bodnarchuk, M. I.; Kovalenko, M. V.; Heiss, W.; Talapin, D. V. *J. Am. Chem. Soc.* **2010**, *132*, 11967−11977.
(13) Vanmaekelbergh, D. *Nano Today* **2011**, *6*, 419−437.
(14) Bishop, K. J. M.; Wilmer, C. E.; Soh, S.; Grzybowski, B. A. *Small* **2009**, *5*, 1600−1630.
(15) Kalsin, A. M.; Fialkowski, M.; Paszewski, M.; Smoukov, S. K.; Bishop, K. J. M.; Grzybowski, B. A. *Science* **2006**, *312*, 420−424.
(16) Dong, A. G.; Chen, J.; Vora, P. M.; Kikkawa, J. M.; Murray, C. B. *Nature* **2010**, *466*, 474−477.
(17) Hickey, R. J.; Koski, J.; Meng, X.; Riggleman, R. A.; Zhang, P.; Park, S.-J. *ACS Nano* **2014**, *8*, 495−502.
(18) Howse, J. R.; Jones, R. A. L.; Battaglia, G.; Ducker, R. E.; Leggett, G. J.; Ryan, A. J. *Nat. Mater.* **2009**, *8*, 507−511.
(19) Park, J.; An, K. J.; Hwang, Y. S.; Park, J. G.; Noh, H. J.; Kim, J. Y.; Park, J. H.; Hwang, N. M.; Hyeon, T. *Nat. Mater.* **2004**, *3*, 891−895.
(20) Mueggenburg, K. E.; Lin, X.-M.; Goldsmith, R. H.; Jaeger, H. M. *Nat. Mater.* **2007**, *6*, 656−660.
(21) Tsapis, N.; Bennett, D.; Jackson, B.; Weitz, D. A.; Edwards, D. A. *Proc. Natl. Acad. Sci. U. S. A.* **2002**, *99*, 12001−12005.
(22) Lacava, J.; Born, P.; Kraus, T. *Nano Lett.* **2012**, *12*, 3279−3282.
(23) Zhang, X.; Zhu, Y.; Granick, S. *Science* **2002**, *295*, 663−666.
(24) Glaser, N.; Adams, D. J.; Boeker, A.; Krausch, G. *Langmuir* **2006**, *22*, 5227−5229.
(25) Yan, J.; Bloom, M.; Bae, S. C.; Luijten, E.; Granick, S. *Nature* **2012**, *491*, 578−581.
(26) Bodnarchuk, M. I.; Kovalenko, M. V.; Groiss, H.; Resel, R.; Reissner, M.; Hesser, G.; Lechner, R. T.; Steiner, W.; Schaeffler, F.; Heiss, W. *Small* **2009**, *5*, 2247−2252.
(27) Liz-Marzán, L. M.; Giersig, M.; Mulvaney, P. *Langmuir* **1996**, *12*, 4329−4335.
(28) Courty, A.; Mermet, A.; Albouy, P. A.; Duval, E.; Pileni, M. P. *Nat. Mater.* **2005**, *4*, 395−398.
(29) Habas, S. E.; Lee, H.; Radmilovic, V.; Somorjai, G. A.; Yang, P. *Nat. Mater.* **2007**, *6*, 692−697.
(30) Zheng, H.; Wang, J.; Lofland, S. E.; Ma, Z.; Mohaddes-Ardabili, L.; Zhao, T.; Salamanca-Riba, L.; Shinde, S. R.; Ogale, S. B.; Bai, F.; Viehland, D.; Jia, Y.; Schlom, D. G.; Wuttig, M.; Roytburd, A.; Ramesh, R. *Science* **2004**, *303*, 661−663.
(31) Rupich, S. M.; Castro, F. C.; Irvine, W. T. M.; Talapin, D. V. *Nat. Commun.* **2014**, *5*, 5045.
(32) Redl, F. X.; Cho, K. S.; Murray, C. B.; O'Brien, S. *Nature* **2003**, *423*, 968−971.
(33) Yang, Z.; Wei, J.; Bonville, P.; Pileni, M.-P. *J. Am. Chem. Soc.* **2015**, *137*, 4487−4493.
(34) Travesset, A. *Proc. Natl. Acad. Sci. U. S. A.* **2015**, *112*, 9563−9567.
(35) Shevchenko, E. V.; Talapin, D. V.; O'Brien, S.; Murray, C. B. *J. Am. Chem. Soc.* **2005**, *127*, 8741−8747.
(36) Chen, J.; Ye, X.; Murray, C. B. *ACS Nano* **2010**, *4*, 2374−2381.
(37) Yang, Z.; Wei, J.; Pileni, M.-P. *Chem. Mater.* **2015**, *27*, 2152−2157.
(38) Wei, J.; Schaeffer, N.; Pileni, M.-P. *J. Am. Chem. Soc.* **2015**, *137*, 14773−14784.
(39) Eldridge, M. D.; Madden, P. A.; Frenkel, D. *Mol. Phys.* **1993**, *79*, 105−120.
(40) Guizar-Sicairos, M.; Thurman, S. T.; Fienup, J. R. *Opt. Lett.* **2008**, *33*, 156−158.
(41) Gilbert, P. *J. Theor. Biol.* **1972**, *36*, 105−117.
(42) Palenstijn, W. J.; Batenburg, K. J.; Sijbers, J. *J. Struct. Biol.* **2011**, *176*, 250−253.
(43) van Aarle, W.; Palenstijn, W. J.; De Beenhouwer, J.; Altantzis, T.; Bals, S.; Batenburg, K. J.; Sijbers, J. *Ultramicroscopy* **2015**, *157*, 35−47.
(44) Zanaga, D.; Bleichrodt, F.; Altantzis, T.; Winckelmans, N.; Palenstijn, W. J.; Sijbers, J.; de Nijs, B.; van Huis, M. A.; Sanchez-Iglesias, A.; Liz-Marzan, L. M.; van Blaaderen, A.; Joost Batenburg, K.; Bals, S.; Van Tendeloo, G. *Nanoscale* **2016**, *8*, 292−299.
(45) Schlossmacher, P.; Klenov, D. O.; Freitag, B.; von Harrach, H. S. E. *Microsc. Today* **2010**, *18*, 14−20.